Upper limit map of a background of gravitational waves

B. Abbott,[14] R. Abbott,[14] R. Adhikari,[14] J. Agresti,[14] P. Ajith,[2] B. Allen,[2, 51] R. Amin,[18] S. B. Anderson,[14]
W. G. Anderson,[51] M. Arain,[39] M. Araya,[14] H. Armandula,[14] M. Ashley,[4] S. Aston,[38] P. Aufmuth,[35] C. Aulbert,[1]
S. Babak,[1] S. Ballmer,[14] H. Bantilan,[8] B. C. Barish,[14] C. Barker,[16] D. Barker,[16] B. Barr,[40] P. Barriga,[50]
M. A. Barton,[40] K. Bayer,[15] K. Belczynski,[24] J. Betzwieser,[15] P. T. Beyersdorf,[27] B. Bhawal,[14] I. A. Bilenko,[21]
G. Billingsley,[14] R. Biswas,[51] E. Black,[14] K. Blackburn,[14] L. Blackburn,[15] D. Blair,[50] B. Bland,[16] J. Bogenstahl,[40]
L. Bogue,[17] R. Bork,[14] V. Boschi,[14] S. Bose,[52] P. R. Brady,[51] V. B. Braginsky,[21] J. E. Brau,[43] M. Brinkmann,[2]
A. Brooks,[37] D. A. Brown,[14, 6] A. Bullington,[30] A. Bunkowski,[2] A. Buonanno,[41] O. Burmeister,[2] D. Busby,[14]
R. L. Byer,[30] L. Cadonati,[15] G. Cagnoli,[40] J. B. Camp,[22] J. Cannizzo,[22] K. Cannon,[51] C. A. Cantley,[40]
J. Cao,[15] L. Cardenas,[14] M. M. Casey,[40] G. Castaldi,[46] C. Cepeda,[14] E. Chalkey,[40] P. Charlton,[9] S. Chatterji,[14]
S. Chelkowski,[2] Y. Chen,[1] F. Chiadini,[45] D. Chin,[42] E. Chin,[50] J. Chow,[4] N. Christensen,[8] J. Clark,[40] P. Cochrane,[2]
T. Cokelaer,[7] C. N. Colacino,[38] R. Coldwell,[39] R. Conte,[45] D. Cook,[16] T. Corbitt,[15] D. Coward,[50] D. Coyne,[14]
J. D. E. Creighton,[51] T. D. Creighton,[14] R. P. Croce,[46] D. R. M. Crooks,[40] A. M. Cruise,[38] A. Cumming,[40]
J. Dalrymple,[31] E. D'Ambrosio,[14] K. Danzmann,[35, 2] G. Davies,[7] D. DeBra,[30] J. Degallaix,[50] M. Degree,[30]
T. Demma,[46] V. Dergachev,[42] S. Desai,[32] R. DeSalvo,[14] S. Dhurandhar,[13] M. Díaz,[33] J. Dickson,[4] A. Di Credico,[31]
G. Diederichs,[35] A. Dietz,[7] E. E. Doomes,[29] R. W. P. Drever,[5] J.-C. Dumas,[50] R. J. Dupuis,[14] J. G. Dwyer,[10]
P. Ehrens,[14] E. Espinoza,[14] T. Etzel,[14] M. Evans,[14] T. Evans,[17] S. Fairhurst,[7, 14] Y. Fan,[50] D. Fazi,[14] M. M. Fejer,[30]
L. S. Finn,[32] V. Fiumara,[45] N. Fotopoulos,[51] A. Franzen,[35] K. Y. Franzen,[39] A. Freise,[38] R. Frey,[43] T. Fricke,[44]
P. Fritschel,[15] V. V. Frolov,[17] M. Fyffe,[17] V. Galdi,[46] J. Garofoli,[16] I. Gholami,[1] J. A. Giaime,[17, 18] S. Giampanis,[44]
K. D. Giardina,[17] K. Goda,[15] E. Goetz,[42] L. Goggin,[14] G. González,[18] S. Gossler,[4] A. Grant,[40] S. Gras,[50]
C. Gray,[16] M. Gray,[4] J. Greenhalgh,[26] A. M. Gretarsson,[11] R. Grosso,[33] H. Grote,[2] S. Grunewald,[1] M. Guenther,[16]
R. Gustafson,[42] B. Hage,[35] D. Hammer,[51] C. Hanna,[18] J. Hanson,[17] J. Harms,[2] G. Harry,[15] E. Harstad,[43]
T. Hayler,[26] J. Heefner,[14] I. S. Heng,[40] A. Heptonstall,[40] M. Heurs,[2] M. Hewitson,[2] S. Hild,[35] E. Hirose,[31]
D. Hoak,[17] D. Hosken,[37] J. Hough,[40] E. Howell,[50] D. Hoyland,[38] S. H. Huttner,[40] D. Ingram,[16] E. Innerhofer,[15]
M. Ito,[43] Y. Itoh,[51] A. Ivanov,[14] D. Jackrel,[30] B. Johnson,[16] W. W. Johnson,[18] D. I. Jones,[47] G. Jones,[7] R. Jones,[40]
L. Ju,[50] P. Kalmus,[10] V. Kalogera,[24] D. Kasprzyk,[38] E. Katsavounidis,[15] K. Kawabe,[16] S. Kawamura,[23]
F. Kawazoe,[23] W. Kells,[14] D. G. Keppel,[14] F. Ya. Khalili,[21] C. Kim,[24] P. King,[14] J. S. Kissel,[18] S. Klimenko,[39]
K. Kokeyama,[23] V. Kondrashov,[14] R. K. Kopparapu,[18] D. Kozak,[14] B. Krishnan,[1] P. Kwee,[35] P. K. Lam,[4]
M. Landry,[16] B. Lantz,[30] A. Lazzarini,[14] B. Lee,[50] M. Lei,[14] J. Leiner,[52] V. Leonhardt,[23] I. Leonor,[43] K. Libbrecht,[14]
P. Lindquist,[14] N. A. Lockerbie,[48] M. Longo,[45] M. Lormand,[17] M. Lubinski,[16] H. Lück,[35, 2] B. Machenschalk,[1]
M. MacInnis,[15] M. Mageswaran,[14] K. Mailand,[14] M. Malec,[35] V. Mandic,[14] S. Marano,[45] S. Márka,[10]
J. Markowitz,[15] E. Maros,[14] I. Martin,[40] J. N. Marx,[14] K. Mason,[15] L. Matone,[10] V. Matta,[45] N. Mavalvala,[15]
R. McCarthy,[16] D. E. McClelland,[4] S. C. McGuire,[29] M. McHugh,[20] K. McKenzie,[4] J. W. C. McNabb,[32]
S. McWilliams,[22] T. Meier,[35] A. Melissinos,[44] G. Mendell,[16] R. A. Mercer,[39] S. Meshkov,[14] E. Messaritaki,[14]
C. J. Messenger,[40] D. Meyers,[14] E. Mikhailov,[15] S. Mitra,[13] V. P. Mitrofanov,[21] G. Mitselmakher,[39] R. Mittleman,[15]
O. Miyakawa,[14] S. Mohanty,[33] G. Moreno,[16] K. Mossavi,[2] C. MowLowry,[4] A. Moylan,[4] D. Mudge,[37] G. Mueller,[39]
S. Mukherjee,[33] H. Müller-Ebhardt,[2] J. Munch,[37] P. Murray,[40] E. Myers,[16] J. Myers,[16] G. Newton,[40]
A. Nishizawa,[23] K. Numata,[22] B. O'Reilly,[17] R. O'Shaughnessy,[24] D. J. Ottaway,[15] H. Overmier,[17] B. J. Owen,[32]
Y. Pan,[41] M. A. Papa,[1, 51] V. Parameshwaraiah,[16] P. Patel,[14] M. Pedraza,[14] S. Penn,[12] V. Pierro,[46] I. M. Pinto,[46]
M. Pitkin,[40] H. Pletsch,[51] M. V. Plissi,[40] F. Postiglione,[45] R. Prix,[1] V. Quetschke,[39] F. Raab,[16] D. Rabeling,[4]
H. Radkins,[16] R. Rahkola,[43] N. Rainer,[2] M. Rakhmanov,[32] S. Ray-Majumder,[51] V. Re,[38] H. Rehbein,[2] S. Reid,[40]
D. H. Reitze,[39] L. Ribichini,[2] R. Riesen,[17] K. Riles,[42] B. Rivera,[16] N. A. Robertson,[14, 40] C. Robinson,[7]
E. L. Robinson,[38] S. Roddy,[17] A. Rodriguez,[18] A. M. Rogan,[52] J. Rollins,[10] J. D. Romano,[7] J. Romie,[17] R. Route,[30]
S. Rowan,[40] A. Rüdiger,[2] L. Ruet,[15] P. Russell,[14] S. Ryan,[16] S. Sakata,[23] M. Samidi,[14] L. Sancho de la Jordana,[36]
V. Sandberg,[16] V. Sannibale,[14] S. Saraf,[25] P. Sarin,[15] B. S. Sathyaprakash,[7] S. Sato,[23] P. R. Saulson,[31] R. Savage,[16]
P. Savov,[6] S. Schediwy,[50] R. Schilling,[2] R. Schnabel,[2] R. Schofield,[43] B. F. Schutz,[1, 7] P. Schwinberg,[16] S. M. Scott,[4]
A. C. Searle,[4] B. Sears,[14] F. Seifert,[2] D. Sellers,[17] A. S. Sengupta,[7] P. Shawhan,[41] D. H. Shoemaker,[15] A. Sibley,[17]
J. A. Sidles,[49] X. Siemens,[14, 6] D. Sigg,[16] S. Sinha,[30] A. M. Sintes,[36, 1] B. J. J. Slagmolen,[4] J. Slutsky,[18]
J. R. Smith,[2] M. R. Smith,[14] K. Somiya,[2, 1] K. A. Strain,[40] D. M. Strom,[43] A. Stuver,[32] T. Z. Summerscales,[3]
K.-X. Sun,[30] M. Sung,[18] P. J. Sutton,[14] H. Takahashi,[1] D. B. Tanner,[39] M. Tarallo,[14] R. Taylor,[14] R. Taylor,[40]
J. Thacker,[17] K. A. Thorne,[32] K. S. Thorne,[6] A. Thüring,[35] K. V. Tokmakov,[40] C. Torres,[33] C. Torrie,[40]
G. Traylor,[17] M. Trias,[36] W. Tyler,[14] D. Ugolini,[34] C. Ungarelli,[38] K. Urbanek,[30] H. Vahlbruch,[35]
M. Vallisneri,[6] C. Van Den Broeck,[7] M. Varvella,[14] S. Vass,[14] A. Vecchio,[38] J. Veitch,[40] P. Veitch,[37] A. Villar,[14]

C. Vorvick,[16] S. P. Vyachanin,[21] S. J. Waldman,[14] L. Wallace,[14] H. Ward,[40] R. Ward,[14] K. Watts,[17]
D. Webber,[14] A. Weidner,[2] M. Weinert,[2] A. Weinstein,[14] R. Weiss,[15] S. Wen,[18] K. Wette,[4] J. T. Whelan,[1]
D. M. Whitbeck,[32] S. E. Whitcomb,[14] B. F. Whiting,[39] C. Wilkinson,[16] P. A. Willems,[14] L. Williams,[39]
B. Willke,[35, 2] I. Wilmut,[26] W. Winkler,[2] C. C. Wipf,[15] S. Wise,[39] A. G. Wiseman,[51] G. Woan,[40] D. Woods,[51]
R. Wooley,[17] J. Worden,[16] W. Wu,[39] I. Yakushin,[17] H. Yamamoto,[14] Z. Yan,[50] S. Yoshida,[28] N. Yunes,[32]
M. Zanolin,[15] J. Zhang,[42] L. Zhang,[14] C. Zhao,[50] N. Zotov,[19] M. Zucker,[15] H. zur Mühlen,[35] and J. Zweizig[14]

(The LIGO Scientific Collaboration, http://www.ligo.org)

[1] Albert-Einstein-Institut, Max-Planck-Institut für Gravitationsphysik, D-14476 Golm, Germany
[2] Albert-Einstein-Institut, Max-Planck-Institut für Gravitationsphysik, D-30167 Hannover, Germany
[3] Andrews University, Berrien Springs, MI 49104 USA
[4] Australian National University, Canberra, 0200, Australia
[5] California Institute of Technology, Pasadena, CA 91125, USA
[6] Caltech-CaRT, Pasadena, CA 91125, USA
[7] Cardiff University, Cardiff, CF2 3YB, United Kingdom
[8] Carleton College, Northfield, MN 55057, USA
[9] Charles Sturt University, Wagga Wagga, NSW 2678, Australia
[10] Columbia University, New York, NY 10027, USA
[11] Embry-Riddle Aeronautical University, Prescott, AZ 86301 USA
[12] Hobart and William Smith Colleges, Geneva, NY 14456, USA
[13] Inter-University Centre for Astronomy and Astrophysics, Pune - 411007, India
[14] LIGO - California Institute of Technology, Pasadena, CA 91125, USA
[15] LIGO - Massachusetts Institute of Technology, Cambridge, MA 02139, USA
[16] LIGO Hanford Observatory, Richland, WA 99352, USA
[17] LIGO Livingston Observatory, Livingston, LA 70754, USA
[18] Louisiana State University, Baton Rouge, LA 70803, USA
[19] Louisiana Tech University, Ruston, LA 71272, USA
[20] Loyola University, New Orleans, LA 70118, USA
[21] Moscow State University, Moscow, 119992, Russia
[22] NASA/Goddard Space Flight Center, Greenbelt, MD 20771, USA
[23] National Astronomical Observatory of Japan, Tokyo 181-8588, Japan
[24] Northwestern University, Evanston, IL 60208, USA
[25] Rochester Institute of Technology, Rochester, NY 14623, USA
[26] Rutherford Appleton Laboratory, Chilton, Didcot, Oxon OX11 0QX United Kingdom
[27] San Jose State University, San Jose, CA 95192, USA
[28] Southeastern Louisiana University, Hammond, LA 70402, USA
[29] Southern University and A&M College, Baton Rouge, LA 70813, USA
[30] Stanford University, Stanford, CA 94305, USA
[31] Syracuse University, Syracuse, NY 13244, USA
[32] The Pennsylvania State University, University Park, PA 16802, USA
[33] The University of Texas at Brownsville and Texas Southmost College, Brownsville, TX 78520, USA
[34] Trinity University, San Antonio, TX 78212, USA
[35] Universität Hannover, D-30167 Hannover, Germany
[36] Universitat de les Illes Balears, E-07122 Palma de Mallorca, Spain
[37] University of Adelaide, Adelaide, SA 5005, Australia
[38] University of Birmingham, Birmingham, B15 2TT, United Kingdom
[39] University of Florida, Gainesville, FL 32611, USA
[40] University of Glasgow, Glasgow, G12 8QQ, United Kingdom
[41] University of Maryland, College Park, MD 20742 USA
[42] University of Michigan, Ann Arbor, MI 48109, USA
[43] University of Oregon, Eugene, OR 97403, USA
[44] University of Rochester, Rochester, NY 14627, USA
[45] University of Salerno, 84084 Fisciano (Salerno), Italy
[46] University of Sannio at Benevento, I-82100 Benevento, Italy
[47] University of Southampton, Southampton, SO17 1BJ, United Kingdom
[48] University of Strathclyde, Glasgow, G1 1XQ, United Kingdom
[49] University of Washington, Seattle, WA, 98195
[50] University of Western Australia, Crawley, WA 6009, Australia
[51] University of Wisconsin-Milwaukee, Milwaukee, WI 53201, USA
[52] Washington State University, Pullman, WA 99164, USA

(Dated: May 1, 2007)

We searched for an anisotropic background of gravitational waves using data from the LIGO S4 science run and a method that is optimized for point sources. This is appropriate if, for example, the gravitational wave background is dominated by a small number of distinct astrophysical sources. No signal was seen. Upper limit maps were produced assuming two different power laws for the source strain power spectrum. For an f^{-3} power law and using the 50 Hz to 1.8kHz band the upper limits on the source strain power spectrum vary between $1.2 \times 10^{-48} \mathrm{Hz}^{-1} \left(100 \ \mathrm{Hz}/f\right)^3$ and $1.2 \times 10^{-47} \mathrm{Hz}^{-1} \left(100 \ \mathrm{Hz}/f\right)^3$, depending on the position in the sky. Similarly, in the case of constant strain power spectrum, the upper limits vary between $8.5 \times 10^{-49} \mathrm{Hz}^{-1}$ and $6.1 \times 10^{-48} \mathrm{Hz}^{-1}$. As a side product a limit on an isotropic background of gravitational waves was also obtained. All limits are at the 90% confidence level. Finally, as an application, we focused on the direction of Sco-X1, the closest low-mass X-ray binary. We compare the upper limit on strain amplitude obtained by this method to expectations based on the X-ray luminosity of Sco-X1.

I. INTRODUCTION

A stochastic background of gravitational waves can be non-isotropic if, for example, the dominant source of stochastic gravitational waves comes from an ensemble of astrophysical sources (e.g. [9, 11]), and if this ensemble is dominated by its strongest members. So far the LIGO Scientific Collaboration has analyzed the data from the first science runs for a stochastic background of gravitational waves [1, 2, 3], assuming that this background is *isotropic*. If astrophysical sources indeed dominate this background, one should look for anisotropies.

A method that is optimized for extreme anisotropies, namely point sources of stochastic gravitational radiation, was presented in [7]. It is based on the cross-correlation of the data streams from two spatially separated gravitational wave interferometers, and is referred to as radiometer analysis. We have analyzed the data of the 4th LIGO science run using this method.

Section II is a short description of the radiometer analysis method. The peculiarities of the S4 science run are summarized in section III, and we discuss the results in section IV.

II. METHOD DESCRIPTION

A stochastic background of gravitational waves can be distinguished from other sources of detector noise by cross-correlating two independent detectors. Thus we cross-correlate the data streams from a pair of detectors with a cross-correlation kernel Q, chosen to be optimal for a source which is specified by an assumed strain power spectrum $H(f)$ and angular power distribution $P(\hat{\Omega})$. Specifically, with $\tilde{s}_1(f)$ and $\tilde{s}_2(f)$ representing the Fourier transforms of the strain outputs of two detectors, this cross-correlation is computed in the frequency domain segment by segment as:

$$Y_t = \int_{-\infty}^{\infty} df \, \tilde{s}_1^*(f) \, Q_t(f) \, \tilde{s}_2(f). \tag{1}$$

In contrast to the isotropic analysis the optimal filter Q_t is now sidereal time dependent. It has the general form:

$$Q_t(f) = \lambda_t \frac{\int_{S^2} d\hat{\Omega} \gamma_{\hat{\Omega},t}(f) P(\hat{\Omega}) H(f)}{P_1(f) P_2(f)} \tag{2}$$

where λ_t is a normalization factor, P_1 and P_2 are the strain noise power spectra of the two detectors, H is the strain power spectrum of the stochastic signal we search for, and the factor $\gamma_{\hat{\Omega},t}$ takes into account the sidereal time dependent time delay due to the detector separation and the directionality of the acceptance of the detector pair. Assuming that the source is unpolarized, $\gamma_{\hat{\Omega},t}$ is given by:

$$\gamma_{\hat{\Omega},t}(f) = \frac{1}{2} \sum_A e^{i2\pi f \hat{\Omega} \cdot \frac{\overrightarrow{\Delta x}}{c}} \ F_1^A(\hat{\Omega}) F_2^A(\hat{\Omega}) \tag{3}$$

where $\overrightarrow{\Delta x} = \overrightarrow{x}_2 - \overrightarrow{x}_1$ is the detector separation vector, $\hat{\Omega}$ is the unit vector specifying the sky position and

$$F_i^A(\hat{\Omega}) = e_{ab}^A(\hat{\Omega}) \frac{1}{2} (\hat{X}_i^a \hat{X}_i^b - \hat{Y}_i^a \hat{Y}_i^b) \tag{4}$$

is the response of detector i to a zero frequency, unit amplitude, $A = +$ or $\times$ polarized gravitational wave. $e_{ab}^A(\hat{\Omega})$ is the spin-two polarization tensor for polarization A and $\hat{X}_i^a$ and $\hat{Y}_i^a$ are unit vectors pointing in the directions of the detector arms (see [6] for details). The sidereal time dependence enters through the rotation of the earth, affecting $\hat{X}_i^a$, $\hat{Y}_i^a$ and $\overrightarrow{\Delta x}$.

The optimal filter Q_t is derived assuming that the intrinsic detector noise is Gaussian and stationary over the measurement time, uncorrelated between detectors, and uncorrelated with and much greater in power than the stochastic gravitational wave signal. Under these assumptions the expected variance, $\sigma_{Y_t}^2$, of the cross-correlation is dominated by the noise in the individual detectors, whereas the expected value of the cross-correlation Y_t depends on the stochastic background power spectrum:

$$\sigma_{Y_t}^2 \equiv \langle Y_t^2 \rangle - \langle Y_t \rangle^2 \approx \frac{T}{4} (Q_t, Q_t) \tag{5}$$

$$\langle Y_t \rangle = T \left(Q_t, \frac{\int_{S^2} d\hat{\Omega} \gamma_{\hat{\Omega},t} P(\hat{\Omega}) H}{P_1 P_2} \right) \qquad (6)$$

Here the scalar product $(\cdot, \cdot)$ is defined as $(A, B) = \int_{-\infty}^{\infty} A^*(f) B(f) P_1(f) P_2(f) df$ and T is the duration of the measurement.

Equation 2 defines the optimal filter Q_t for any arbitrary choice of $P(\hat{\Omega})$. To optimize the method for finite, but unresolved astrophysical sources one should use a $P(\hat{\Omega})$ that covers only a localized patch in the sky. But the angular resolution is diffraction limited with the detector separation as baseline and the frequency content weighted by $H^2 P_1^{-1} P_2^{-1}$. For a constant $H(f)$ this corresponds to a resolution of several tens of square degrees, so that astrophysical sources will not be spatially resolved. Thus we chose to optimize the method for true point sources, i.e. $P(\hat{\Omega}) = \delta^2(\hat{\Omega}, \hat{\Omega}')$, which also allows for a more efficient implementation (see [7]).

We define the strain power spectrum $H(f)$ of a point source as one-sided (positive frequencies only) and including the power in both polarizations. Thus $H(f)$ is related to the gravitational luminosity L_{GW} and the gravitational energy flux $F(f)$ through

$$L_{GW} = \int_{f_{\min}}^{f_{\max}} F(f) df = \frac{c^3 \pi}{4G} \int_{f_{\min}}^{f_{\max}} H(f) f^2 df, \qquad (7)$$

with c the light speed and G Newton's constant. We look for strain power spectra $H(f)$ in the form of a power law with exponent β. The amplitude at the pivot point of 100 Hz is described by H_β, i.e.

$$H(f) = H_\beta \left(\frac{f}{100 \text{ Hz}} \right)^\beta. \qquad (8)$$

With this definition we can choose the normalization of the optimal filter Q_t such that equation 6 reduces to

$$\langle Y_t \rangle = H_\beta. \qquad (9)$$

The data set from a given interferometer pair is divided into equal-length intervals, and the cross-correlation Y_t and theoretical σ_{Y_t} are calculated for each interval, yielding a set $\{Y_t, \sigma_{Y_t}\}$ of such values for each sky direction $\hat{\Omega}$, with t the mid-segment sidereal time. The optimal filter Q_t is kept constant and equal to its mid-segment value for the whole segment. The remaining error due to this discretization is of second order in $(T_{\text{seg}}/1 \text{ day})$ and is given by:

$$\begin{aligned} Y_{\text{err}}(T_{\text{seg}})/Y &= \frac{T_{\text{seg}}^2}{24} \frac{\int_{-\infty}^{\infty} \frac{\partial^2 \gamma_{\hat{\Omega}'}^*}{\partial t^2} \gamma_{\hat{\Omega}'} \frac{H^2}{P_1 P_2} df}{\int_{-\infty}^{\infty} |\gamma_{\hat{\Omega}'}|^2 \frac{H^2}{P_1 P_2} df} \\ &= O\left(\left(\frac{2\pi f d}{c} \frac{T_{\text{seg}}}{1 \text{ day}} \right)^2 \right) \end{aligned} \qquad (10)$$

with f the typical frequency and d the detector separation. At the same time the interval length can be chosen such that the detector noise is relatively stationary over one interval. We use an interval length of 60 sec, which guarantees that the relative error $Y_{\text{err}}(T_{\text{seg}})/Y$ is less than 1%. The cross-correlation values are combined to produce a final cross-correlation estimator, Y_{opt}, that maximizes the signal-to-noise ratio, and has variance σ_{opt}^2:

$$Y_{\text{opt}} = \sum_t \sigma_{Y_t}^{-2} Y_t / \sigma_{\text{opt}}^{-2}, \qquad \sigma_{\text{opt}}^{-2} = \sum_t \sigma_{Y_t}^{-2}. \qquad (11)$$

In practice the intervals are overlapping by 50% to avoid the effective loss of half the data due to the required windowing (Hanning). Thus equation 11 was modified slightly to take the correlation of neighboring segments into account.

The data was downsampled to 4096 Hz and high-pass filtered with a sixth order Butterworth filter with a cutoff frequency at 40 Hz. Frequencies between 50 Hz and 1800 Hz were used for the analysis and the frequency bin width was 0.25 Hz. Frequency bins around multiples of 60 Hz up to the tenth harmonic were removed, along with bins near a set of nearly monochromatic injected signals used to simulate pulsars. These artificial pulsars proved useful in a separate end-to-end check of this analysis pipeline, which successfully recovered the sky locations, frequencies and strengths of three such pulsars listed in TABLE I. The resulting map for one of these pulsars is shown in FIG. 5.

III.   THE LIGO S4 SCIENCE RUN

The LIGO S4 science run consisted of one month of co-incident data taking with all three LIGO interferometers (22 Feb 2005 noon to 23 Mar 2005 midnight CST). During that time all three interferometers where roughly a factor of 2 in amplitude away from design sensitivity over almost the whole frequency band. Also, the Livingston interferometer was equipped with a Hydraulic External Pre-Isolation (HEPI) system, allowing it to stay locked during day time. This made S4 the first LIGO science run with all-day coverage at both sites. A more detailed description of the LIGO interferometers is given in [5].

Since the radiometer analysis requires two spatially separated sites we used only data from the two 4 km interferometers (H1 in Hanford and L1 in Livingston). For these two interferometers about 20 days of coincident data was collected, corresponding to a duty factor of 69%.

The large spatial separation also reduces environmental correlations between the two sites. Nevertheless we still found a comb of 1 Hz harmonics that was coherent between H1 and L1. This correlation was found to be at least in part due to an exactly 1-sec periodic signal in both interferometers (FIG. 1), which was caused by cross-talk from the GPS_RAMP signal. The GPS_RAMP signal consists of a 10 msec saw-tooth signal that starts at every full second, lasts for 1 msec and is synchronized with the GPS receivers. (see FIG. 1). This ramp was

Injected pulsars			
Quantity	Pulsar #3	Pulsar #4	Pulsar #8
Frequency during S4 run	108.86 Hz	1402.20 Hz	193.94 Hz
Noise level (σ)	1.89×10^{-47}	6.04×10^{-46}	1.73×10^{-47}
Injected Hdf (corrected for polarization)	1.74×10^{-46}	4.28×10^{-44}	1.54×10^{-46}
Recovered Hdf on source	1.74×10^{-46}	4.05×10^{-44}	1.79×10^{-46}
Signal-to-noise ratio (SNR)	9.2	67.1	10.3
Injected position	11h 53m 29.4s	18h 39m 57.0s	23h 25m 33.5s
	$-33° \ 26' \ 11.8''$	$-12° \ 27' \ 59.8''$	$-33° \ 25' \ 6.7''$
Recovered position (max SNR)	12h 12m	18h 40m	23h 16m
	$-37°$	$-13°$	$-32°$

TABLE I: **Injected pulsars:** The table shows the level at which the three strongest injected pulsars were recovered. Hdf denotes the RMS strain power over the 0.5 Hz band that was used. The reported values of for the injected Hdf include corrections that account for the difference between the polarized pulsar injection and an unpolarized source that is expected by the analysis. The underestimate of Pulsar #4 is due to a known bias of the analysis method in the case of a signal strong enough to affect the power spectrum estimation.

used as an off-line monitor of the Analog-to-Digital Converter (ADC) card timing and thus was connected to the same ADC card that was used for the gravitational wave channel, which resulted in a non-zero cross-talk to the gravitational wave channel.

To reduce the contamination from this signal a transient template was subtracted in the time domain. This has the advantage that effectively only a very narrow band (1/runtime $\approx 1 \times 10^{-6}$ Hz) is removed around each 1 Hz harmonic, while the rest of the analysis is unaffected. The waveform for subtraction from the raw (uncalibrated) data was recovered by averaging the data from the whole run in order to produce a typical second. Additionally, since this typical second only showed significant features in the first 80 msec, the transient subtraction template was set to zero (with a smooth transition) after 120 msec. This subtraction was done for only H1 since adding repetitive data to both detectors can introduce artificial correlation. It eliminated the observed correlation. However, due to an automatically adjusted gain between the ADC card and the gravitational wave channel, the amplitude of the transient waveform is affected by a residual systematic error. Its effect on the cross-correlation result was estimated by comparing maps with the subtraction done on either H1 or L1. The systematic error is mostly concentrated around the north and south poles, with a maximum of about 50% of the statistical error at the south pole. In the declination range of $-75°$ to $+75°$ the error is less than 10% of the statistical error. For upper limit calculations this systematic error is added in quadrature to the statistical error. After the S4 run the GPS_RAMP signal was replaced with a two-tone signal at 900 Hz and 901 Hz. The beat between the two is now used to monitor the timing.

One post-processing cut was required to deal with detector non-stationarity. To avoid a bias in the cross-correlation statistics the segment before and the segment after the one being analyzed are used for the power spectral density (PSD) estimate [10]. Therefore the analysis

becomes vulnerable to large, short transients that happen in one instrument in the middle segment - such transients cause a significant underestimate of the PSD and thus of the theoretical standard deviation for this segment. This leads to a contamination of the final estimate.

To eliminate this problem the standard deviation σ is estimated for both the middle segment and the two adjacent segments. The two estimates are then required to agree within 20%:

$$\frac{1}{1.2} < \frac{\sigma_{\text{middle}}}{\sigma_{\text{adjacent}}} < 1.2. \quad (12)$$

The analysis is fairly insensitive to the threshold - the only significant contamination comes from very large outliers that are cut by any reasonable threshold [8]. The chosen threshold of 20% eliminates less than 6 % of the data.

IV. RESULTS FROM THE S4 RUN

A. Broadband results

In this analysis we searched for an $H(f)$ following a power law with two different exponents β:

- $\beta = -3$: $H(f) = H_{-3} \left(\frac{100 \text{ Hz}}{f} \right)^3$.
  This emphasizes low frequencies and is useful when interpreting the result in a cosmological framework, since it corresponds to a scale-invariant primordial perturbation spectrum, i.e. the GW energy per logarithmic frequency interval is constant.

- $\beta = 0$: $H(f) = H_0$ *(constant strain power)*.
  This emphasizes the frequencies for which the interferometer strain sensitivity is highest.

The results are reported as point estimate $Y_{\hat{\Omega}}$ and corresponding standard deviation $\sigma_{\hat{\Omega}}$ for each pixel $\hat{\Omega}$. The
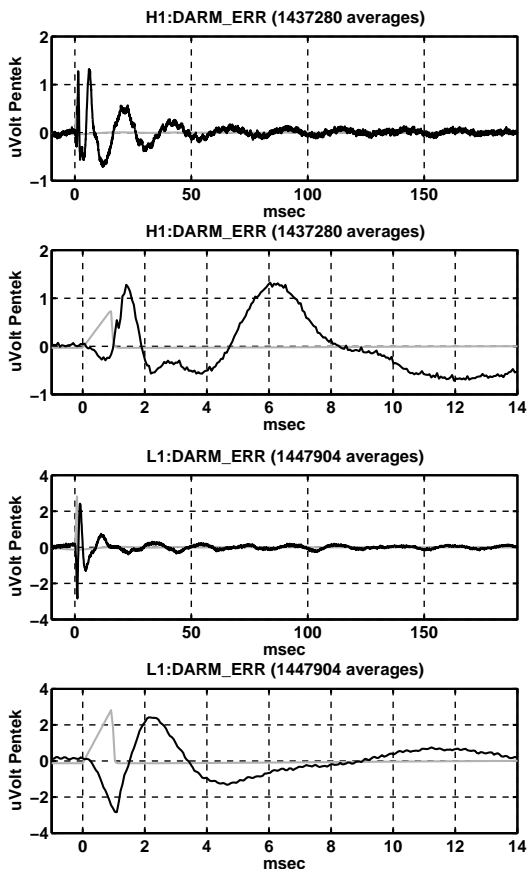
FIG. 1: **Periodic timing transient** in the gravitational wave channel (DARM_ERR), calibrated in μVolt at the ADC (Pentek card) for H1 (top two) and L1 (bottom two) shown with a span of 200 msec and 14 msec in black. The x-axis is the offset from a full GPS second. About 1.4 million seconds of DARM_ERR data was averaged to get this trace. Also shown in gray is the GPS_RAMP signal that was used as a timing monitor. It was identified as a cause of the periodic timing transient in DARM_ERR. The H1 trace shows an additional feature at 6 msec.

point estimate $Y_{\hat{\Omega}}$ must be interpreted as best fit amplitude H_β for the pixel $\hat{\Omega}$ (equation 9).

Also we should note that the resulting maps have an intrinsic spatial correlation, which is described by the point spread function

$$A(\hat{\Omega}, \hat{\Omega}') = \frac{\langle Y_{\hat{\Omega}} Y_{\hat{\Omega}'} \rangle}{\langle Y_{\hat{\Omega}'} Y_{\hat{\Omega}'} \rangle}. \tag{13}$$

It describes the spatial correlation in the following sense: if either $Y_{\hat{\Omega}'} = \bar{Y}$ due to random fluctuations, or if there is a true source of strength $\bar{Y}$ at $\hat{\Omega}'$, then the expectation value at $\hat{\Omega}$ is $\langle Y_{\hat{\Omega}} \rangle = A(\hat{\Omega}, \hat{\Omega}')\bar{Y}$. The shape of $A(\hat{\Omega}, \hat{\Omega}')$ depends strongly on the declination. FIG. 4 shows $A(\hat{\Omega}, \hat{\Omega}')$ for different source declinations and both the $\beta = -3$ and $\beta = 0$ case, assuming continuous day coverage.

1. Scale-invariant case, $\beta = -3$
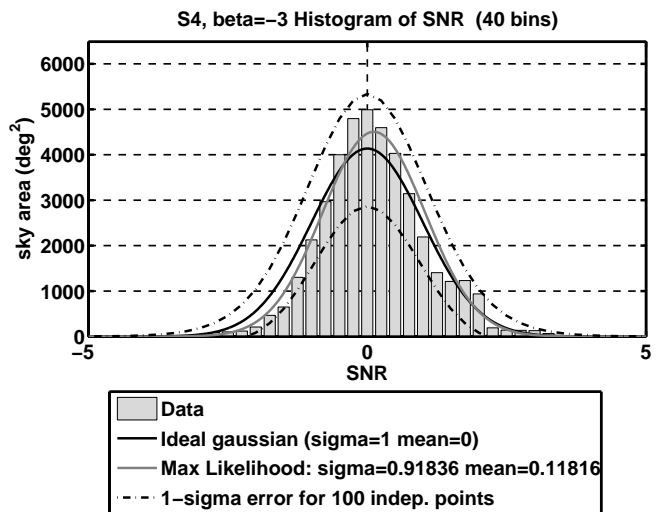
FIG. 2: **S4 Result:** Histogram of the signal-to-noise ratio (SNR) for $\beta = -3$. The gray curve is a maximum likelihood Gaussian fit to the data. The black solid line is an ideal Gaussian, the two dash-dotted black lines indicate the expected one sigma variations around this ideal Gaussian for 100 independent points ($N_{\text{eff}} = 100$).

A histogram of the SNR $= \frac{Y}{\sigma}$ is plotted in FIG. 2. The data points were weighted with the corresponding sky area in square degrees. Because neighboring points are correlated, the effective number of independent points N_{eff} is reduced. Therefore the histogram can exhibit statistical fluctuations that are significantly larger than those naively expected from simply counting the number of pixels in the map, while still being consistent with (correlated) Gaussian noise. Indeed the histogram in FIG. 2 features a slight bump around SNR=2, but is still consistent with $N_{\text{eff}} = 100$ - the red dash-dotted lines indicate the one sigma band around the red ideal Gaussian for $N_{\text{eff}} = 100$. Additionally the SNR distribution also passes a Kolmogorov-Smirnov test for $N_{\text{eff}} = 100$ at the 90% significance level.

The number of independent points N_{eff}, which in effect describes the diffraction limit of the LIGO detector pair, was estimated by 2 heuristic methods:

- *Spherical harmonics decomposition* of the SNR map. The resulting power vs l graph shows structure up to roughly $l = 9$ and falls off steeply above that - the $l = 9$ point corresponds to one twentieth of the maximal power. The effective number of independent points then is $N_{\text{eff}} \approx (l+1)^2 = 100$.

- *FWHM area* of a strong injected source, which is latitude dependent but of the order of 800 square degrees. To fill the sky we need about $N_{\text{eff}} \approx 50$ of those patches. We used the higher estimate $N_{\text{eff}} = 100$ for this discussion.

FIG. 2 suggests that the data is consistent with no signal. Thus we calculated a Bayesian 90% upper limit for each sky direction. The prior was assumed to be flat between zero and an upper cut-off set to $5 \times 10^{-45} \mathrm{Hz}^{-1}$ at 100 Hz, the approximate limit that can be set from just operating a single LIGO interferometer at the S4 sensitivity. Note, however, that this cut-off is so high that the upper limit is completely insensitive to it. Additionally we marginalized over the calibration uncertainty of 8% for H1 and 5% for L1 using a Gaussian probability distribution. The resulting upper limit map is shown in FIG. 6. The upper limits on the strain power spectrum $H(f)$ vary between $1.2 \times 10^{-48} \mathrm{Hz}^{-1} (100 \mathrm{~Hz}/f)^3$ and $1.2 \times 10^{-47} \mathrm{Hz}^{-1} (100 \mathrm{~Hz}/f)^3$, depending on the position in the sky. These strain limits correspond to limits on the gravitational wave energy flux $F(f)$ varying between $3.8 \times 10^{-6} \mathrm{erg} \mathrm{~cm}^{-2} \mathrm{~Hz}^{-1} (100 \mathrm{~Hz}/f)$ and $3.8 \times 10^{-5} \mathrm{erg} \mathrm{~cm}^{-2} \mathrm{~Hz}^{-1} (100 \mathrm{~Hz}/f)$.

2. Constant strain power, $\beta = 0$

Similarly, FIG. 3 shows a histogram of the SNR $= \frac{Y}{\sigma}$ for the constant strain power case. Structure in the spherical harmonics power spectrum goes up to $l = 19$, thus N_{eff} was estimated to be $N_{\mathrm{eff}} \approx (l+1)^2 = 400$. Alternatively the FWHM area of a strong injection covers about $100°^2$ which also leads to $N_{\mathrm{eff}} \approx 400$. The dash-dotted red lines in the histogram (FIG. 3) correspond to the expected $1-\sigma$ deviations from the ideal Gaussian for $N_{\mathrm{eff}} = 400$. The histogram is thus consistent with (correlated) Gaussian noise, indicating that there is no signal present. The SNR distribution also passes a Kolmogorov-Smirnov test for $N_{\mathrm{eff}} = 400$ at the 90% significance level.

Again we calculated a Bayesian 90% upper limit for each sky direction, including the marginalization over the calibration uncertainty. The prior was again assumed to be flat between 0 and an upper cut-off of $5 \times 10^{-45} \mathrm{Hz}^{-1}$ at 100 Hz. The resulting upper limit map is shown in FIG. 7. The upper limits on the strain power spectrum $H(f)$ vary between $8.5 \times 10^{-49} \mathrm{Hz}^{-1}$ and $6.1 \times 10^{-48} \mathrm{Hz}^{-1}$ depending on the position in the sky. This corresponds to limits on the gravitational wave energy flux $F(f)$ varying between $2.7 \times 10^{-6} \mathrm{erg} \mathrm{~cm}^{-2} \mathrm{~Hz}^{-1} (f/100 \mathrm{~Hz})^2$ and $1.9 \times 10^{-5} \mathrm{erg} \mathrm{~cm}^{-2} \mathrm{~Hz}^{-1} (f/100 \mathrm{~Hz})^2$.

3. Interpretation

The maps presented in FIGS. 6 and 7 represent the first directional upper limits on a stochastic gravitational wave background ever obtained. They are consistent with no gravitational wave background being present. This search is optimized for well localized, broadband sources of gravitational waves. As such it is best suited for unexpected, poorly modeled sources.
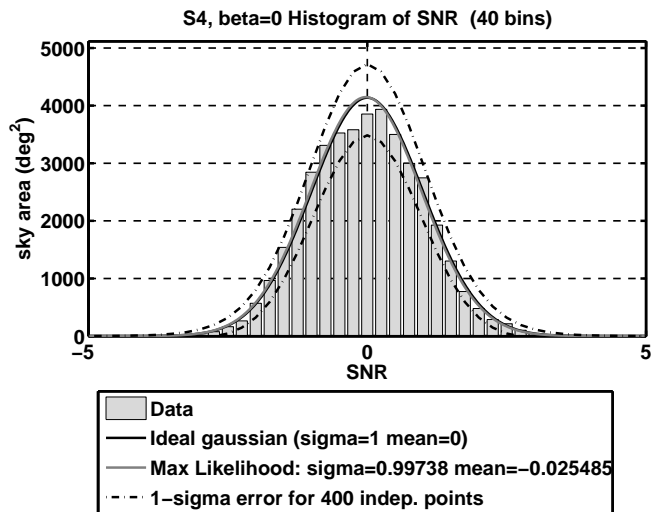

FIG. 3: **S4 Result:** Histogram of the signal-to-noise ratio (SNR) for $\beta = 0$. The gray curve is a maximum likelihood Gaussian fit to the data. The black solid line is an ideal Gaussian, the two dash-dotted black lines indicate the expected one sigma variations around this ideal Gaussian for 400 independent points ($N_{\mathrm{eff}} = 400$).

In order to compare the result to what could be expected from known sources we also search for the gravitational radiation from low-mass X-ray binaries (LMXBs). They are accretion-driven spinning neutron stars, i.e. narrow-band sources and thus not ideal for this broadband search. However they have the advantage that we can predict the gravitational luminosity based on the known X-ray flux. If gravitational radiation provides the torque balance for LMXBs, then there is a simple relation between the gravitational luminosity L_{GW} and X-ray luminosity L_X [13]:

$$L_{GW} \approx \frac{f_{\mathrm{spin}}}{f_{\mathrm{Kepler}}} L_X. \qquad (14)$$

Here f_{Kepler} is final orbital frequency of the accreting matter, about 2 kHz for a neutron star, and f_{spin} is the spin frequency.

As an example we estimate the gravitational luminosity of all LMXBs within the Virgo galaxy cluster. Their integrated X-ray luminosity is about 10^{-9} erg/sec/cm^2 (3000 galaxies at 15 Mpc, 10^{40} erg/sec/galaxy from LMXBs). For simplicity we assume that the ensemble produces a flat strain power spectrum $H(f)$ over a bandwidth Δf. Then the strength of this strain power spectrum is about

$$\begin{aligned} H(f) &= \frac{2G}{\pi c^3} \frac{1}{f_{\mathrm{Kepler}} f_{\mathrm{center}} \Delta f} L_X \\ &\approx 10^{-55} \mathrm{~Hz}^{-1} \left(\frac{100 \mathrm{~Hz}}{f_{\mathrm{center}}}\right)\left(\frac{100 \mathrm{~Hz}}{\Delta f}\right). \end{aligned} \qquad (15)$$

Here f_{center} is the typical frequency of the Δf wide band of interest. This is quite a bit weaker than the upper limit

set in this paper, which is mostly due to the fact that the intrinsically narrow-band sources are diluted over a broad frequency band.
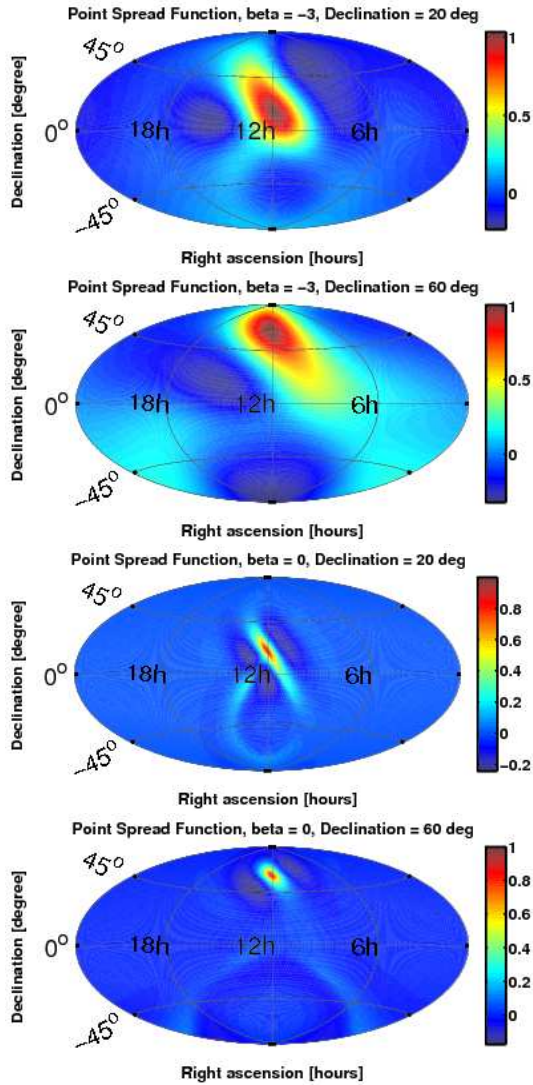

FIG. 4: **Point spread function** $A(\hat{\Omega}, \hat{\Omega}')$ of the radiometer for $\beta = -3$ (top two figures) and for $\beta = 0$ (bottom two figures). Plotted is the relative expected signal strength assuming a source at right ascension $12\,h$ and declinations $20°$ and $60°$. Uniform day coverage was assumed, so the resulting shapes are independent of right ascension. An Aitoff projection was used to plot the whole sky.

B. Limits on isotropic background

It is possible to recover the estimate for an isotropic background as an integral over the map (see [7]). The corresponding theoretical standard deviation would require a double integral with essentially the point spread function as integrand. In practice it is simpler to calculate this theoretical standard deviation directly by using the
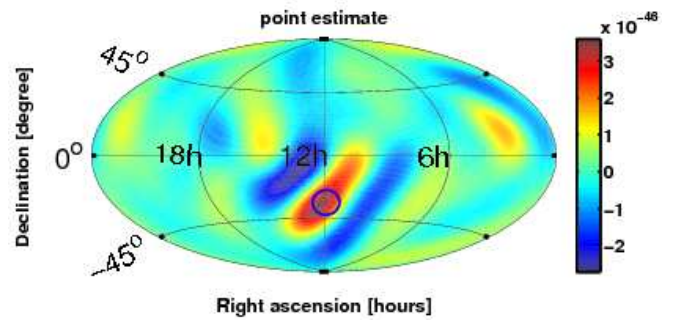
FIG. 5: **Injected pulsar #3:** The analysis was run using the $108.625\,\text{Hz} - 109.125\,\text{Hz}$ frequency band. The artificial signal of Pulsar #3 at 108.86 Hz stands out with a signal-to-noise ratio of 9.2. The circle marks the position of the simulated pulsar.
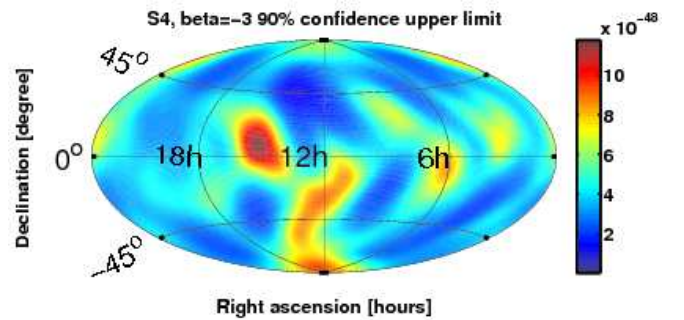
FIG. 6: **S4 Result:** Map of the 90% confidence level Bayesian upper limit on H_β for $\beta = -3$. The upper limit varies between $1.2 \times 10^{-48}\text{Hz}^{-1}(100\,\text{Hz}/f)^3$ and $1.2 \times 10^{-47}\text{Hz}^{-1}(100\,\text{Hz}/f)^3$, depending on the position in the sky. All fluctuations are consistent with the expected noise.
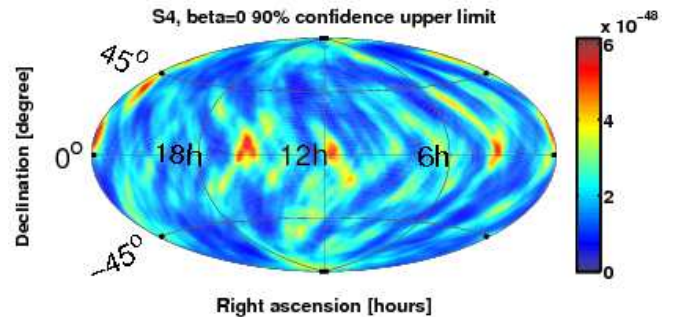

FIG. 7: **S4 Result:** Map of the 90% confidence level Bayesian upper limit on H_β for $\beta = 0$. The upper limit varies between $8.5 \times 10^{-49}\text{Hz}^{-1}$ and $6.1 \times 10^{-48}\text{Hz}^{-1}$ depending on the position in the sky.

overlap reduction function for an isotropic background (see [6]). From that the 90% Bayesian upper limit can be calculated, which is additionally marginalized over the calibration uncertainty. In the $\beta = -3$ case the 90% up-

per limit we can set on $h_{72}^2\Omega_{\text{gw}}(f)$ is 1.20×10^{-4}. The dimensionless quantity $\Omega_{\text{gw}}(f)$ is the GW energy density per unit logarithmic frequency, divided by the critical energy density ρ_c to close the universe, and h_{72} is the Hubble constant in units of 72 km sec^{-1}Mpc^{-1}. Table II summarizes the results for all choices of β.

1. Interpretation

In [1] we published an upper limit of $h_{72}^2\Omega_{GW} < 6.5 \times 10^{-5}$ on an isotropic gravitational wave background using S4 data. That analysis is mathematically identical to inferring the point estimate as an integral over the map [7], but the mitigation of the timing transient and the data quality cuts were sufficiently different to affect the point estimate. While both results are consistent within the error bar of the measurement, this difference results in a slightly higher upper limit. Both results are significantly better than the previously published LIGO S3 result.

C. Narrow-band results targeted on Sco-X1

As an application we again focus on low-mass X-ray binaries (LMXBs). The gravitational wave flux from all LMXBs is expected to be dominated by the closest one, Sco-X1, simply because Sco-X1 dominates the X-ray flux from all LMXBs, and X-ray luminosity L_X is related to the gravitational luminosity L_{GW} through equation 14. Unfortunately the spin frequency of Sco-X1 is not known. We thus want to set an upper limit for each frequency bin on the RMS strain coming from the direction of Sco-X1 (RA: 16h 19m 55.0850s; Dec: -15° 38' 24.9").

The binary orbital velocity of Sco-X1 is about 40 ± 5 km/sec (see [12]). This induces a maximal frequency shift of $\Delta f_{GW} = 2.7 \times 10^{-4} \times f_{GW}$. We chose a bin width of $df = 0.25$ Hz, which is broader than maximal frequency shift Δf_{GW} for all frequencies below 926 Hz and is the same bin width that was used for the broadband analysis. Above 926 Hz the signal is guaranteed to spread over multiple bins.

To avoid contamination from the hardware-injected pulsars, the 2 frequency bins closest to a pulsar frequency were excluded. Multiples of 60 Hz were also excluded. The lowest frequency bin was at 50 Hz, the highest one at 1799.75 Hz. FIG. 8 shows a histogram of the remaining 6965 0.25 Hz wide frequency bins. It is consistent with a Gaussian distribution (Kolmogorov-Smirnov test with $N = 6965$ at the 90% significance level).

A 90% Bayesian upper limit for each frequency bin was calculated based on the point estimate and standard deviation, including a marginalization over the calibration uncertainty. Figure 9 is a plot of this 90% limit (red trace). Above about 200 Hz (shot noise regime above the cavity pole) the typical upper limit rises linearly with fre-
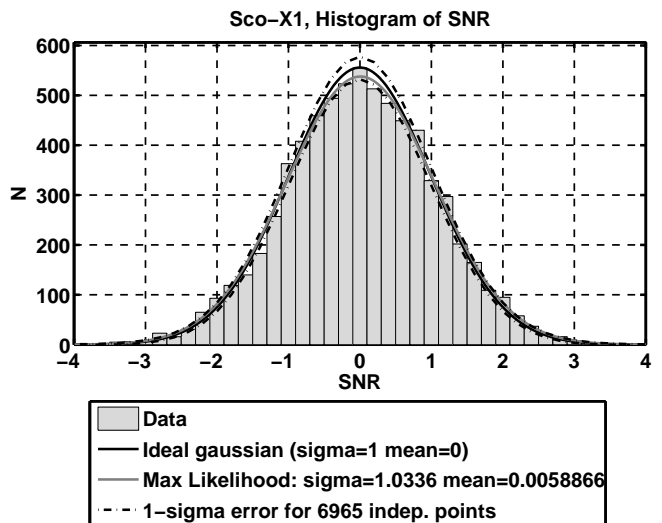

FIG. 8: **S4 Result for Sco-X1:** Histogram of the signal-to-noise ratio calculated for each 0.25 Hz wide frequency bin. There are no outliers.
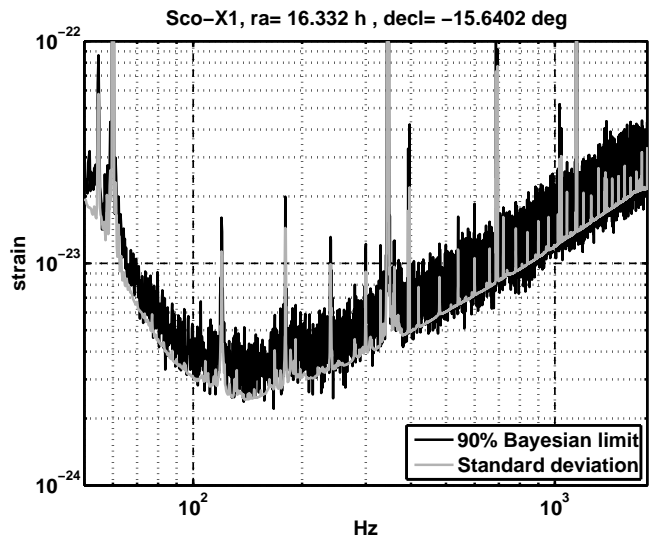

FIG. 9: **S4 Result for Sco-X1:** The 90% confidence Bayesian upper limit as a function of frequency - marginalized over the calibration uncertainty. The standard deviation (one sigma error bar) is shown in blue.

quency and is given by

$$h_{\text{RMS}}^{(90\%)} \approx 3.4 \times 10^{-24} \left(\frac{f}{200 \text{ Hz}}\right) \quad f \gtrsim 200 \text{ Hz}. \quad (16)$$

The standard deviation is also shown in blue.

1. Interpretation

In principle, the radiometer analysis is not an optimal method to search for a presumably periodic source like

S4 isotropic upper limit

Quantity	$\Omega_{\mathrm{gw}}(f) = const$	$S_{\mathrm{gw}}(f) = const$
point estimate Y	$1.02 \times 10^{-47} \mathrm{Hz}^{-1} \left(\frac{f}{100\mathrm{Hz}}\right)^{-3}$	$-7.12 \times 10^{-48} \mathrm{Hz}^{-1}$
standard deviation σ	$6.97 \times 10^{-48} \mathrm{Hz}^{-1} \left(\frac{f}{100\mathrm{Hz}}\right)^{-3}$	$7.22 \times 10^{-48} \mathrm{Hz}^{-1}$
90% Bayesian UL on $S_{\mathrm{gw}}(f)$	$1.99 \times 10^{-47} \mathrm{Hz}^{-1} \left(\frac{f}{100\mathrm{Hz}}\right)^{-3}$	$8.49 \times 10^{-48} \mathrm{Hz}^{-1}$
90% Bayesian UL on $h_{72}^2 \Omega_{\mathrm{gw}}(f)$	1.20×10^{-4}	$5.13 \times 10^{-5} \left(\frac{f}{100\mathrm{Hz}}\right)^{3}$

TABLE II: **S4 isotropic result** for the $\Omega_{\mathrm{gw}}(f) = const$, $(\beta = -3)$ and the $S_{\mathrm{gw}}(f) = const$, $(\beta = 0)$ case. The first two lines show the point estimate and standard deviation that are used to calculate the 90% Bayesian upper limits. The upper limits are also marginalized over the calibration uncertainty. These results agree with the ones published in [1] within the error bar of the measurement.

Sco-X1. Nevertheless it can set a competitive upper limit with a minimal set of assumptions on the source and significantly less computational resources. Indeed LIGO published a 95% upper limit on gravitational radiation amplitude from Sco-X1 of 1.7×10^{-22} to 1.3×10^{-21} across the $464 - 484$ Hz and $604 - 624$ Hz frequency bands [4], using data from S2, which had a noise amplitude about 4.5 times higher around 500 Hz in each instrument. The analysis was computationally limited to using 6 hours of data and two 20 Hz frequency bands. However the strain amplitude sensitivity scales as $T^{-1/4}$ [7], while a coherent method scales as $T^{-1/2}$.

The upper limit (eq. 16) can directly be compared to the expected strain based on the X-ray luminosity:

$$\frac{h_{\mathrm{RMS}}^{(90\%)}}{h_{\mathrm{RMS}}^{L_X}} \approx 100 \left(\frac{f}{200 \text{ Hz}}\right)^{\frac{3}{2}} \quad f \gtrsim 200 \text{ Hz}. \quad (17)$$

Here f is the gravitational wave frequency, i.e. twice the (unknown) spin frequency of Sco-X1. This is close enough that, if the model described in [13], and thus equation 14 are indeed correct, Sco-X1 ought to be detectable with this method and the next generation of gravitational wave detectors operated in a narrow-band configuration (AdvLIGO [14]). For a discussion of the expected signal from Sco-X1 see also [4].

V. CONCLUSION

We produced the first upper limit maps for a stochastic gravitational wave background by applying a method that is described in [7] to the data from the LIGO S4 science run. No signal was seen and upper limits were set for two different choices for the strain power spectrum $H(f)$. In the case of $H(f) \propto f^{-3}$ the upper limits for a point source vary between $1.2 \times 10^{-48} \mathrm{Hz}^{-1} (100 \text{ Hz}/f)^3$ and $1.2 \times 10^{-47} \mathrm{Hz}^{-1} (100 \text{ Hz}/f)^3$, depending on the position in the sky (see FIG. 6). Similarly, in the case of constant $H(f)$ the upper limits vary between $8.5 \times 10^{-49} \mathrm{Hz}^{-1}$ and $6.1 \times 10^{-48} \mathrm{Hz}^{-1}$ (see FIG. 7). As a side product limits

on an isotropic background of gravitational waves were also obtained, see TABLE II.

In an additional application, narrow-band upper limits were set on the gravitational radiation coming from the closest low-mass X-ray binary, Sco-X1 (see FIG. 9). In the shot noise limited frequency band (above about 200 Hz) the limits on the strain in each 0.25 Hz wide frequency bin follow roughly

$$h_{\mathrm{RMS}}^{(90\%)} \approx 3.4 \times 10^{-24} \left(\frac{f}{200 \text{ Hz}}\right) \quad f \gtrsim 200 \text{ Hz}, \quad (18)$$

where f is the gravitational wave frequency (twice the spin frequency).

[1] B. Abbott *et al.*, astro-ph/0608606, to be published in ApJ.

[2] B. Abbott *et al.*, Phys. Rev. Lett. **95**, 221101 (2005).

[3] B. Abbott *et al.*, Phys. Rev. D **69**, 122004 (2004).

[4] B. Abbott *et al.*, gr-qc/0605028, to be published in PRD.

[5] B. Abbott *et al.*, Nucl. Instrum. Methods A**517** (2004) 154-179.

[6] B. Allen and J.D. Romano, Phys. Rev. D **59**, 102001 (1999).

[7] S.W. Ballmer, Class. Quantum Grav. **23**, S179-S185 (2006).

[8] S.W. Ballmer, MIT thesis (2006).

[9] L. Bildsten, Astrophys. J. **501** L89-L93 (1998)

[10] A. Lazzarini, J. Romano LIGO preprint (2004) http://www.ligo.caltech.edu/docs/T/T040089-00.pdf

[11] T. Regimbau, J. A. de Freitas Pacheco Astron. Astrophys. **376**, 381 (2001)

[12] D. Steeghs, J. Cesares, Astrophys. J. **568**, 273 (2002)

[13] R. V. Wagoner, Astrophys. J. **278**, 345 (1984)

[14] http://www.ligo.caltech.edu/advLIGO/